DNS of a Shock Wave-Boundary Layer Interaction on a Ramp with Surface Roughness

Giuseppe Chiapparino [1], Christian Stemmer [2]

Abstract

Direct Numerical Simulations are performed to investigate roughness effects on a Mach 6 hypersonic compression-corner flow. Different variants of a roughness patch placed upstream of the boundary-layer smooth separation point are considered. The patches consist of sinusoidal elements, with modifications in position and spanwise extension of the roughness. Compared to a smooth-wall case, all the rough cases cause a delayed boundary-layer separation and hence a smaller recirculation bubble. Moreover, the roughness-induced streamwise vorticity, which is convected downstream by the detached shear layer, generates mushroom-like structures once the flow reattaches on the ramp. The properties of such structures, although similar, reflect the character of the patch upstream of the bubble. The roughness inducing the locally largest flow distortion is responsible for the widest structure on the ramp, characterized by the highest increase in wall-temperature peak. The patch occupying the entire width of the domain generate instead the weakest vortices on the ramp.

Keywords: *Hypersonic boundary-layer flow, roughness patch, separation region, compression corner*

Nomenclature

Latin
h − Enthalpy
L − Length
M − Mach number
p − Pressure
q − Heat flux
Pr − Prandtl number
Re − Reynolds number
Re_{kk} − Roughness Reynolds number
St − Stanton number
T − Temperature
u − Streamwise velocity
w − Spanwise velocity
Greek
γ − Heat-capacity ratio
δ − Boundary-layer thickness

θ − Ramp angle
λ − Thermal conductivity
μ − Dynamic viscosity
ρ − Density
ω − Vorticity

Superscripts
C − Value at the core (of the vortex)
W − Value at the wall
$\circ$ − Total quantity

Subscripts
∞ − Freestream conditions
k − Value at roughness position
r − Value at reattachment location
s − Value at separation location
w − Value at the wall

1. Introduction

The ramp geometry is a simple configuration used to model engine intakes and control flaps of high-speed vehicles, such as scramjets and Shuttle-like re-entry vehicles. Typically, hypersonic conditions are achieved at high altitudes, where ambient pressure and density are very low compared to sea-level

[1]*Chair of Aerodynamics and Fluid Mechanics, Technical University of Munich, Germany, Giuseppe.Chiapparino@tum.de*

[2]*Chair of Aerodynamics and Fluid Mechanics, Technical University of Munich, Germany, Christian.Stemmer@tum.de*

conditions. Nevertheless, the vehicle high speed leads to the formation of strong shock waves close to the vehicle surfaces, thus imposing intense mechanical and thermal stresses on the vehicle itself. Under these conditions, the pressure and temperature values in proximity of the surfaces could become high enough to even promote chemical reactions within the flow, such as molecular dissociation and recombination, with further effects on the vehicle [1]. The exact flow topology resulting from the interaction between the freestream and the vehicle depends on the geometry of the vehicle. In particular, the ramp configuration induces a strong oblique shock-wave, which interacts with the incoming boundary layer. The consequent Shock-Wave/Boundary-Layer Interaction (SWBLI) [2] might lead to boundary-layer separation well upstream of the compression corner. In this case, a separation shock forms where the flow detaches. The separated shear layer then convects downstream and eventually reattaches on the ramp, where a reattachment shock forms. Confined by the two shocks, the shear layer and the wall, there is the recirculation (or separation) bubble. In two-dimensional ramp geometries, the separation bubble can host secondary separations that lead to the consequent formation of multiple vortices in the recirculation region [3, 4, 5]. Such phenomenon is more evident for long separation bubbles, which are comparable to the length of the flat part in front of the ramp [6]. For given freestream conditions, the higher the ramp angle is, the longer the separation bubble becomes. When secondary vortices are present in the recirculation region, the Stanton number and skin-friction distributions at the wall show secondary peaks as well in correspondence to these smaller vortices. However, if the ramp angle exceeds certain values the separation bubble might become unstable and, with the introduction of freestream disturbances upstream of the boundary-layer separation, the flow shows a three-dimensional behaviour. The reattachment line exhibits a corrugated pattern, with streamlines generating nodes and saddle points in its proximity, and streamwise streaks form in the fully reattached flow [7, 8]. Amplification can eventually lead to transition further downstream along the ramp. Similar to the ramp-induced SWBLI is the case of an impinging shock over a flat plate. Provided that the boundary layer experiences a comparable pressure rise due to the incoming shock, the flow behaviour is equivalent to the one on the ramp [2]. In this case, the length of the separation bubble scales with the impinging-shock angle. Hence, such flow configurations may become unstable for high impinging angles [9, 10] and the critical modes can be computed, for example, by means of global stability analysis.

In ramp-induced SWBLI, the conditions of the incoming boundary layer have a strong influence on the flow interaction. A thicker boundary layer separates more easily than a thinner one, leading to larger separation bubbles. Hence, cooling the wall upstream of the compression corner or flying at a higher Mach number makes the bubble shrink. A similar effect can be obtained by having a fully turbulent boundary-layer interacting with the ramp. In this case, however, the wall heat-flux is stronger than in a laminar interaction. And for transitional flows, even higher rates can be achieved [11]. Boundary-layer transition may happen naturally over smooth walls or may be induced by surface roughness, which might be intentional (trips) or the result of manufacturing imperfections, dirt, small gaps/steps between tiles or ablation. For high-speed boundary layers, a roughness element needs to be very high with respect to the local boundary-layer thickness in order to cause immediate transition (i.e. to be "effective"). Experimentally [12] it was found that, for Mach 4.8 and 6 flat-plate boundary layers, spherical elements twice as high as the local boundary-layer thickness are needed to trigger immediate transition. The shape of the elements appears to be also a factor affecting the roughness effectiveness, as emerged by experimental comparisons between spherical and triangular elements [13], with the latter becoming effective at lower Reynolds numbers. For lower heights of the roughness elements, transition does not happen immediately, but can be still affected. In these cases, the roughness is said to be "critical" [14], and induces a steady modification of the boundary layer in its wake. Here, the flow can be more unstable than in a smooth-wall case. Hence, freestream disturbances convected in the wake region can grow in amplitude, eventually leading to transition earlier than in the natural case. This was experimentally demonstrated at low speeds [15], where the presence of surface waviness with a well-defined wavenumber spectrum led to an increase of the receptivity coefficients of a Blasius boundary layer excited by TS waves. In hypersonic boundary layers, the effect of isolated roughness elements on flow stability was numerically investigated for a Mach 6 flat plate by analysing different parameters. The wake of a "pizza-box" roughness [16] can sustain the growth of several instabilities, such as odd (sinuous) and even (varicose) modes, leading to a faster boundary-layer transition. The

numerical experiments also showed that cooling the wall had a stabilising effect for all the modes in the roughness wake. For a similar setup [17], several parameters like height, planform, front and streamwise shapes of the roughness were analysed in order to assess their effect on transition. The latter two parameters were the most influential for flow breakdown. Moreover, a direct relation was found between the maximum amplitude of the streaks forming behind the elements and the exponential growth rate of instabilities in the roughness wake. On the experimental side, the investigation of multiple asymmetric isolated elements on a supersonic flat plate [18] showed that the relative position of such elements can have an impact on transition location and stability properties of the wake flow. Often, a critical roughness accelerates the process of transition, moving the location of onset forward closer to the roughness. However, under certain conditions and for elements smaller than the boundary-layer thickness, roughness also seems to be able to slightly delay transition, as suggested by some investigations [12, 19, 20].

In addition to flat-plate geometries, experimental and numerical investigations on the role of roughness in transition mechanisms have been performed for other geometries like cones and blunt bodies [21, 22, 23]. Regarding the ramp configuration, the influence of roughness elements on laminar SWBLI has been investigated in a number of recent works, for both two-dimensional [5, 24] and three-dimensional [25] setups. In the latter case, the effect of an array of roughness elements ahead of successive small compression corners of an engine intake was numerically simulated. Such trips induce the formation of steady mushroom-shaped structures, which become more evident once they pass onto the following ramp. As a consequence, streamwise streaks are produced downstream of the roughness, with effects on the heat flux at the wall. In the wake of the trips, both sinuous and varicose modes were identified, with the former being the most unstable ones. It was concluded that, for trip heights between the critical and effective values, the roughness-induced streak instability might play a role in transition. It is worth noting that, in those investigations [25], the ramp angles were too small to generate clear recirculation regions at the corners. Hence, the effects of the separation bubble could not be taken into account. These effects might play an important role in the amplitudes growth-rates. Moreover, it is known that longer recirculation regions can be unstable to external perturbations [10], and it has been shown that the streamwise deceleration that takes place in the bubble and at reattachment of the shear layer is responsible for amplification of streamwise-velocity perturbations [26].

As mentioned, the characteristics of the separation bubble can be influenced by many factors, roughness being one of them. Hence, it is to be expected that roughness elements would not only influence the base-flow of an hypersonic compression-corner, but would also have an impact on the stability properties of the new base-flow. Therefore, as a first step, the present work investigates the effects induced on the base-flow by a roughness patch placed upstream of an hypersonic compression-corner. In particular, some parameters of the patch, like shape and position, are modified in order to explore the response of the laminar Shock-Wave/Boundary-Layer Interaction to such variations. In future studies, the investigation could be extended to the impact of such modifications on the stability properties of the roughness-affected flow.

2. Methodology

2.1. Setup and Geometry

This work focuses on a $M_\infty = 6$ hypersonic flow over a $\theta = 10°$ compression corner. Freestream conditions, marked with the subscript "∞", are taken at a reference altitude of 25km for standard air and are listed in Table 1.

Table 1. Freestream conditions at reference altitude of 25km.

Parameter	Value	Parameter	Value
T_∞	220 [K]	μ_∞	$1.44 \cdot 10^{-5}$ [Pa·s]
p_∞	2500 [Pa]	ρ_∞	0.0396 [Kg/m^3]
M_∞	6	u_∞	1783.89 [m/s]

The freestream and geometrical conditions considered here represent plausible operational conditions for control surfaces of high-speed aircraft studied over the last years (as in the HEXAFLY-INT project [27]). The dimensions of the computational domain are $L_x = 0.490$m, $L_y = 0.065$m and $L_z = 0.021$m in the streamwise, wall-normal and spanwise directions, respectively. The reference system originates at the inflow, on the lower corner of the domain, as shown by the blue square in Fig. 1a. The compression corner is situated at $L_c = 0.300$m downstream of the inflow. The dimensions of the computational domain are the same for both the smooth and the rough cases. However, in the latter ones, a three-dimensional roughness patch is modelled by directly modifying the grid-surface height at the wall. The roughness consists of a number of streamwise and spanwise sinusoidal elements, and different positions and types of patch are considered. The surface height is computed as

$$y_k(x, z) = k \cdot f_1 \cdot \sin\left[\frac{\pi(x - x_i)}{I_x/E_x}\right] \cdot \sin\left[\frac{\pi(z - z_i)}{I_z/E_z}\right], \tag{1}$$

where I_x and I_z indicate the streamwise length and the spanwise width of the patch, respectively. E_x and E_z represent the number of half-sinusoidal elements in the x- and z-directions. The piecewise function $f_1 = f_1(x, z)$ limits the patch to the rectangular area defined by $[x_i, x_i + I_x]$ and $[z_i, z_i + I_z]$, with $x_i = x_k - I_x/2$ and $z_i = z_k - I_z/2$ being the lower limits of the patch. Four different variants of the patch are considered. In particular, two different streamwise positions are taken into account. The first (labelled $RP1$) is closer to the inflow, while the second ($RP2$) is placed further downstream, but still ahead of the smooth boundary-layer separation point. The centres of those patches are placed at $(x_k, z_k)_{RP1} = (0.0461, 0.0105)m$ and $(x_k, z_k)_{RP2} = (0.0936, 0.0105)m$, respectively. In both positions $RP1$ and $RP2$, an "isolated" roughness (in the sense that the patch covers a very limited portion of the domain) made of respectively 6 and 1 half-sinusoidal elements in streamwise and spanwise direction, as shown in Fig. 1b, is considered. For position $RP2$ only, two further distributed-roughness patches are investigated: the first ($RP2B$, Fig. 2a) consisting in a spanwise stripe of sinusoidal elements, and the second ($RP2C$, Fig. 2b) consisting in a wider version of the $RP2$ patch with 3 spanwise half-sinusoidal elements.
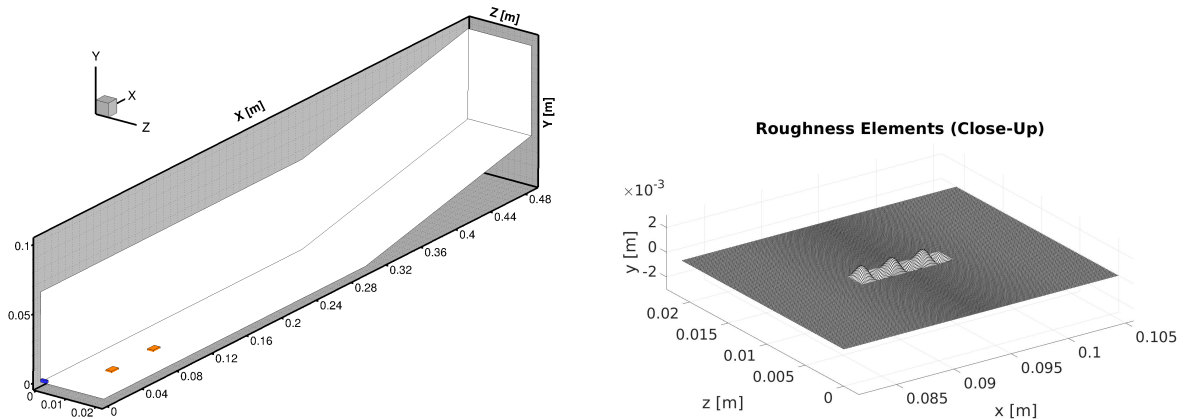
(a) Orange boxes indicate positions $RP2$ and $RP1$.   (b) $RP2$ patch. $RP1$ is identical in shape.

Fig 1. Schematic of the physical domain and detailed view of the base roughness patch.

In all cases, the peak height of the roughness elements is k = 1 mm. For the conditions considered in the present study, this yields a value of the k/δ ratio (δ being the boundary-layer thickness) of 0.621 and 0.439 at $RP1$ and $RP2$, respectively. The corresponding roughness Reynolds numbers, defined as $Re_{kk} = \rho_k u_k k/\mu_k$ (the subscript k denoting flow properties at the roughness height k for a smooth configuration), are about 370 and 150, respectively. Table 2 sums up the geometric parameters of the domain, while Table 3 lists the details of the four roughness variants.
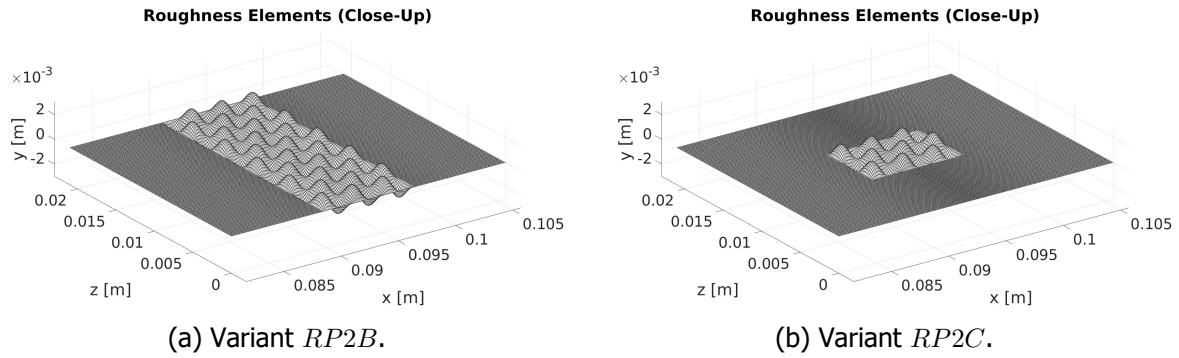
(a) Variant $RP2B$.

(b) Variant $RP2C$.

Fig 2. Detailed view of the two further roughness-patch variants investigated in the present work.

Table 2. Geometric parameters

Parameter	Value	Parameter	Value
L_x	0.400 [m]	L_c	0.300 [m]
L_z	0.021 [m]	θ	10 [°]
L_y	0.065 [m]	k	1 [mm]

2.2. Governing Equations

Direct Numerical Simulations are performed. The compressible three-dimensional Navier–Stokes equations are solved and the ideal gas law is used as closure equation, since the temperatures reached within the domain are not high enough to trigger any considerable chemical reaction. Thus, the heat-capacity ratio γ = 1.4 is constant and is obtained through the standard-air specific-heat coefficients for constant pressure (c_P) and volume (c_V). The temperature-dependent dynamic viscosity (μ) is computed using Sutherland's law with S_1 = 110.3 K, while the thermal conductivity is calculated as $\lambda_T = \mu c_P / Pr$, using a constant Prandtl number Pr = 0.72.

2.3. Numerical Setup and Procedure

The semi-commercial solver Navier-Stokes Multi Block (NSMB) is used to perform the Direct Numerical Simulations. This finite-volume based code has been employed and validated in hypersonic flow calculations in several studies [5, 23, 28, 29, 30] and uses the MPI protocol to allow parallel computations on structured grids with multiple blocks. In the present work, a fourth-order central scheme is used for the spatial discretization, while steady state solutions are achieved through a pseudo-time integration with an implicit Euler scheme based on a lower-upper symmetric Gauss-Seidel method.

The computational grids for both the smooth and the rough cases are similar, though small differences are present. The same number of points is used in streamwise, wall-normal and spanwise directions ($N_x \cdot N_y \cdot N_z$ = 4000·141·256 $\simeq$ 144·10^6 nodes). But while the smooth grid has constant-length streamwise elements, the grid cells of the rough cases are stretched in streamwise direction around the roughness locations. In wall-normal direction, both grids implement a three-layers stretching with the same wall-

Table 3. Patch parameters

Patch	I_x [mm]	I_z [mm]	E_x	E_z
$RP1$	8	2	6	1
$RP2$	8	2	6	1
$RP2B$	8	21	6	10
$RP2C$	8	6	6	3

normal resolution. The three-layers distribution of the nodes allows to refine the grid in the boundary-layer and separation-bubble regions close to the wall. In spanwise direction, a constant spacing of the grid lines is employed. All the grids are divided in 2400 blocks that can be run in parallel on multiple processors. Each grid has six boundaries where the boundary conditions are imposed. At the inflow, Dirichlet conditions with freestream flow values are prescribed. At the outflow and upper part of the domain, in order to avoid undesired wave reflections, characteristic variables with extrapolation in space are imposed. In spanwise direction, periodic boundary conditions are given. At the wall, no-slip boundaries are imposed, together with two surface-temperature conditions: a cold-wall case (T_w = 500 K, only for the smooth case) and an adiabatic wall.

3. Code Validation

The code validation was performed against two cases of hypersonic compression-corner flows, one numerical and one experimental. In the first validation, the reference is represented by the $\theta = 18°$ ramp used in the grid convergence study of [4]. This case consists in a Mach 9.1 flow over a fairly high compression corner, which induces the formation of a long separation region with multiple secondary vortices. Table 4 show the freestream conditions used in the validation case. The original simulation was performed on a two-dimensional $4031 \cdot 1009 \simeq 4 \cdot 10^6$ nodes grid, using a second-order upwind method for spatial discretization. The results from NSMB are obtained with a coarser grid ($3500 \cdot 450 \simeq 1.75 \cdot 10^6$ nodes) but a higher-order method (fourth-order central scheme).

Table 4. Flow conditions and wall temperature from [4].

Parameter	Value	Parameter	Value
T_∞	160 [K]	T_w	350 [K]
p_∞	730 [Pa]	ρ_∞	0.016 [Kg/m^3]
U_∞	2280 [m/s]	Re_∞	$3.22 \cdot 10^6$ [m^{-1}]

Overall, an excellent agreement is obtained. Figs. 3a and 4 show the pressure-coefficient (c_p) distribution at the wall and a detail of the recirculation pattern within the separation bubble, respectively. In NSMB (solid line), an almost identical flow separation is obtained, with reattachment just slightly anticipated. The plateau of the pressure value is consistent with the reference case along the separation region, with a slight discrepancy at reattachment peak. There, NSMB slightly overestimate the pressure coefficient, but the maximum error is within 3%. The development of the secondary vortices inside the bubble is the same, as shown by the streamlines patterns, and so are the compression wave originating from the shear layer at the top of the bubble.
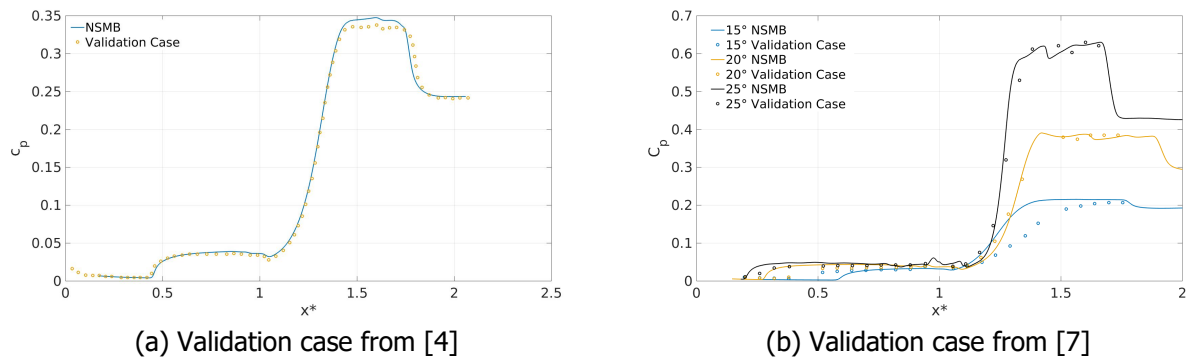

(a) Validation case from [4]

(b) Validation case from [7]

Fig 3. Code validation, pressure-coefficient at the wall for the two selected cases.

For the second validation case, the experimental results obtained in [7] are reproduced with NSMB. The experiments investigate a Mach 7.7 flow over a 3D compression corner, whose angle has been
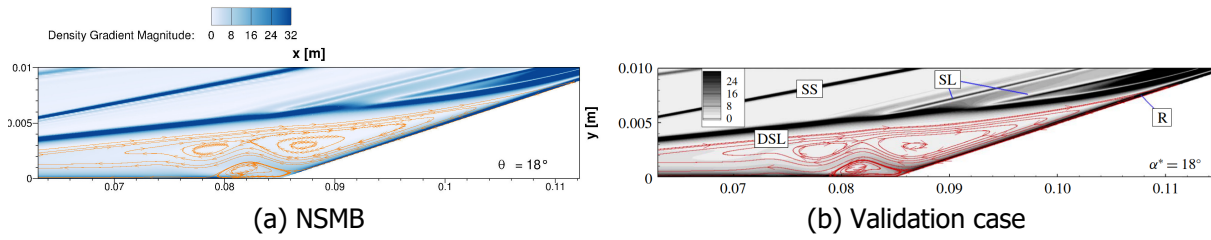
Fig 4. Code validation from [4], secondary vortices within the separation bubble.

set to θ = 15°, 20°, 25° during different experimental runs. The nominal freestream conditions of the experiment are listed in Table 5.

Table 5. Flow conditions and wall temperature from [7].

Parameter	Value	Parameter	Value
T_∞	125 [K]	T_w	293 [K]
p_∞	760 [Pa]	ρ_∞	0.0212 [Kg/m^3]
U_∞	1745 [m/s]	Re_∞	$4.2 \cdot 10^6$ [m^{-1}]

The results from NSMB are obtained on a 2D grid made of $6000 \cdot 450 \simeq 2.7 \cdot 10^6$ nodes, again using the fourth-order central scheme, and are compared to the experimental values taken along the centreline of the models. Fig. 3b shows the pressure-coefficient distribution at the wall. For the higher ramp angles (θ = 20°, 25°), a very good agreement can be observed, especially considering the pressure values at the plateau just downstream of separation and the peak values achieved at reattachment. In particular, the θ = 25° locations where pressure rises due to separation and reattachment are well predicted. In the θ = 20° case, the flow under experimental conditions separates more downstream with respect to the numerical calculation. From the available data, the position of the reattachment peak of this case is not entirely clear, even though the numerical simulation seems to give a reasonable prediction. A poorer agreement is achieved for the smallest ramp angle (θ = 15°). While the separation and reattachment pressure values are ultimately well predicted, the location of these pressure rises do not match the wind-tunnel evidences. However, the experiment shows an almost identical separation position for both θ = 15° and θ = 20° cases (in Fig. 8 of [7], where a logarithmic axis for c_p is used, the two points upstream of x* = 0.5 are separated, but the difference is very small). This seems very peculiar, since the length of the separation bubble should scale with the angle of the ramp, provided that all the other boundary conditions are kept the same. A reasonable explanation for such data could be the lack of streamwise resolution in the pressure measurement, due to the low number of sensors placed upstream of x* = 0.5. Hence, for the case with θ = 15°, the boundary-layer separation (and the consequent pressure rise) seems to take place in between two sensors, resulting in a measurement very similar to the case with θ = 20°. Nevertheless, even taking this problem into account, NSMB still predicts a delayed separation with respect to the experiment.

4. Results

4.1. Smooth reference case

Fig. 5 summarizes the main results for the smooth cases. The background slice shows the pressure contour, the outflow plane shows the streamwise vorticity while the wall is coloured with temperature (adiabatic case) and Stanton-number (cold-wall case) distributions. The thicker blue line at x = 0.300 m in Fig. 5a indicates the corner location. As shown by the pressure contours, a relatively weak shock forms right at the leading edge of the flat plate, at the inflow of the domain. Further downstream, a sharper increase in pressure is visible where the boundary layer separates, at x_s = 0.130 m for adiabatic-wall conditions. In the recirculation region, the pressure is constant, as expected, before undergoing a final

and stronger rise once the flow reattaches on the ramp. The adiabatic-wall condition allows for a non-uniform temperature distribution at the surface (Fig. 5a). Hotter regions can be noticed downstream of separation and just before reattachment. However, the most noticeable increase in temperature is well visible once the flow reattaches on the ramp. Even though the maximum temperatures are in the order of 1600 K, they are too low to trigger relevant chemical reactions within the flow and the ideal-gas assumption is thus acceptable. The black isolines corresponding to a value of streamwise velocity u = -0.1 m/s highlight the corrugated pattern of the reattachment line, in contrast to the straight one at separation point. The mean reattachment position lies around $x_r \simeq 0.435$ m. Clearly visible, the flow characterizing the separation bubble is three-dimensional, despite the formally two-dimensional geometry of the problem, indicating a possible global instability of the flow. Along the ramp downstream of reattachment, six streamwise vortices form, as shown by the vorticity ω_x end-ramp slice. These vortices are characterized by a relatively low strength (at least one order of magnitude smaller than the rough cases), with spanwise velocities of the order of $\pm$ 10 m/s. Nevertheless, their effect on the wall-temperature distribution is visible, as shown in Fig. 5a, where hotter streaks appear on the ramp.

Under cold-wall conditions, the flow shows considerable differences. As expected, the thinner boundary layer entails a delayed separation ($x_s \simeq 0.208$ m) and an early reattachment ($x_r \simeq 0.350$ m) with respect to the adiabatic-wall case. The fixed wall-temperature condition allows to evaluate the heat flux exchanged at the surface by means of the Stanton number, which is defined as

$$St = \frac{q_w}{\rho_\infty U_\infty (h_\infty^\circ - h_w)}, \qquad (2)$$

where $h_\infty^\circ = c_p T_\infty^\circ$ and h_w are the total freestream and the wall enthalpies, respectively. As shown in Fig. 5b, streaks form again downstream of the corrugated reattachment line, while low heat-flux values are detected inside the separation region. Furthermore, it is to note that, once the flow has reattached, streamwise-vorticity levels along the ramp are much higher than those of the adiabatic case.
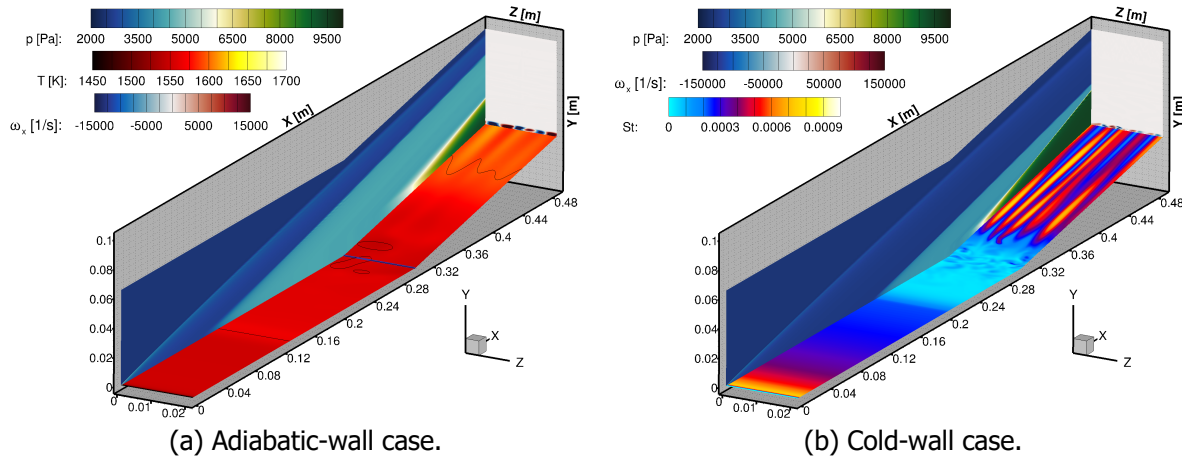

(a) Adiabatic-wall case.   (b) Cold-wall case.

Fig 5. Smooth cases. Pressure contour, wall-temperature distribution, streamwise-vorticity at the outflow and (black) iso-lines showing separation and reattachment positions for the adiabatic-wall case. Pressure contour, wall Stanton-number distribution and streamwise-vorticity for the cold-wall case.

4.2. Rough cases

The roughness patch introduces substantial modifications to the flow field with respect to the smooth wall case. The effects of the patch $RP2$ are analysed first. All the other roughness elements can be seen as variants of case $RP2$, either in location or in shape, and are therefore considered in the next subsections.
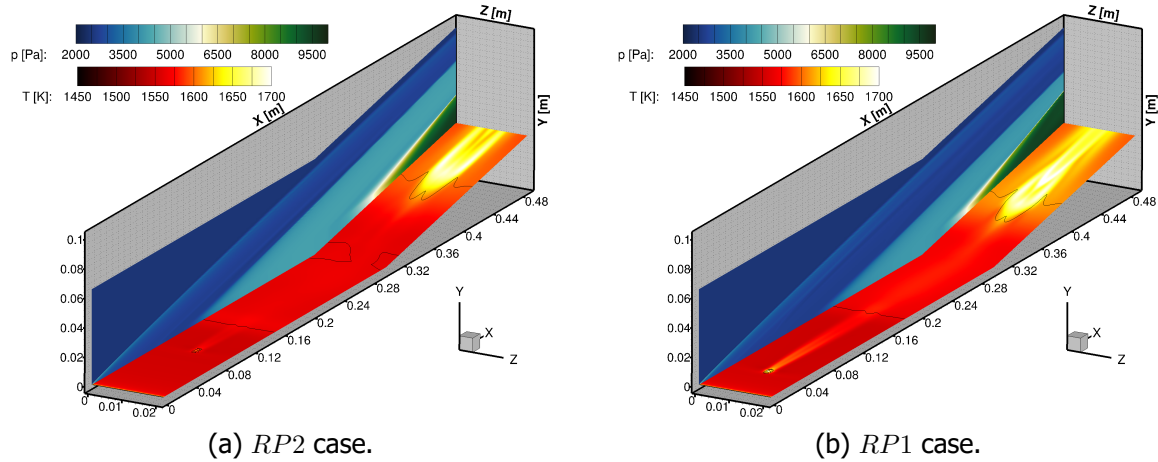
(a) $RP2$ case. (b) $RP1$ case.

Fig 6. $RP2$ and $RP1$ cases. Pressure contour, wall-temperature distribution. Roughness effects are visible in the temperature distribution and flow separation and reattachment (iso-lines).

4.2.1. RP2

First of all, introducing the roughness upstream of the smooth separation-bubble location has an effect on the boundary-layer separation point. As shown in Fig. 6, the recirculation bubble of the rough case is smaller than in the reference case, meaning that the boundary-layer separation is delayed ($x_s \simeq 0.150$ m) and the detached shear layer also reattaches earlier on the ramp. Contrary to the smooth case, the separation line is not straight, but shows a corrugation in the wake of the patch. At reattachment, the roughness induces the formation of a mushroom-shaped structure along the ramp, as shown by the streamwise-velocity contours in Fig. 7a. This structure is a consequence of the streamwise vortices that originate in the wake of the roughness elements and are convected by the detached shear layer over the separation bubble. These vortices are then amplified once reattachment happens on the ramp and push slow flow away from the wall. Once separated from the wall, the flow inside the mushroom gets accelerated by the incoming post-shock ramp flow, as indicated by the change in color of the mushroom core in Fig. 7a. The single streamwise-row of elements in the patch $RP2$ generates one vortical structure on the ramp. The width the double-vortex core (i.e. the "mushroom hat") is $\Delta z^C \simeq 3.3$ mm (1.65 time the patch width) and, once the structure is formed, remains almost constant along the ramp. The streamwise-vorticity trace at the wall, instead, grows in width along the ramp, up to a size of $\Delta z^W \simeq 14$ mm towards the end of the ramp (Fig. 10a).

The effect of this vortical structure is also visible on the wall temperature distribution. A high-temperature streak is present downstream of the roughness patch before separation (even though this temperature rise is quite modest) and a stronger one forms at reattachment, just beneath the mushroom structure. The peak temperature is higher than the reference case (up to $T_w \simeq 1700$ K), but still not high enough for relevant chemistry effects. Finally, Fig. 8 shows the flow topology in the proximity of the roughness. As it encounters the patch, the flow opens up and then closes again in the wake. This motion forms streamwise vortices that lose part of their intensity quite quickly. However, what is left of them convects on the separated shear layer and, as mentioned, amplifies on the ramp, once the flow reattaches, as visible in Fig. 9.

4.2.2. RP1

This patch position is the closest to the domain inflow and the farthest upstream with respect to the smooth separation point. Compared to the previous case, somewhat similar effects are obtained, although some differences stand out with respect to the $RP2$-case. The separation bubble is even smaller than in the $RP2$-case (Fig. 6b). The higher Re_{kk} characterizing the roughness $RP1$ seems associated to a more delayed boundary-layer separation and, as a consequence, an earlier flow reattachment on the ramp. Again, the separation line shows a corrugation in the wake of the patch. The mushroom-shaped

structure on the ramp forms more upstream due to the earlier reattachment and is bigger than in case $RP2$ (Fig. 7b), both in its core ($\Delta z^C \simeq 4.4$ mm) and at the wall ($\Delta z^W \simeq 17$ mm). As the roughness $RP1$ is hit by a thinner boundary-layer, the vorticity forming in the wake of the patch is more widespread and stronger than in the case $RP2$. Moreover, the decay rate of such wake vortices is slower and makes the boundary-layer more resistant to separation. Despite these differences, the peak wall-temperature at reattachment is comparable to the $RP2$ case, reaching around 1710 K. But the streak immediately downstream of the patch is hotter than case $RP2$ due to the higher wake vorticity.

(a) $RP2$ case.
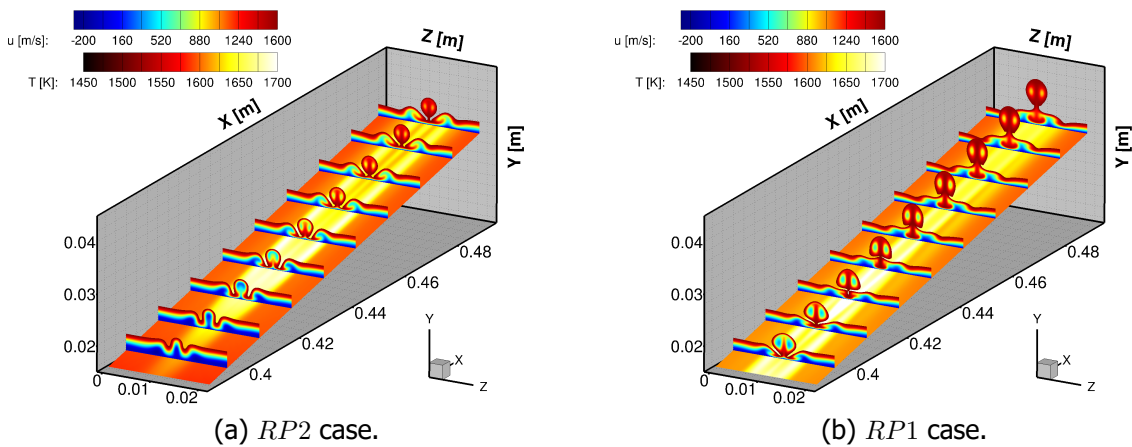
(b) $RP1$ case.

Fig 7. $RP2$ and $RP1$ cases. Evolution of the mushroom-shaped structure along the ramp (streamwise-velocity slices cut above u = 1600 m/s) and wall-temperature distribution.
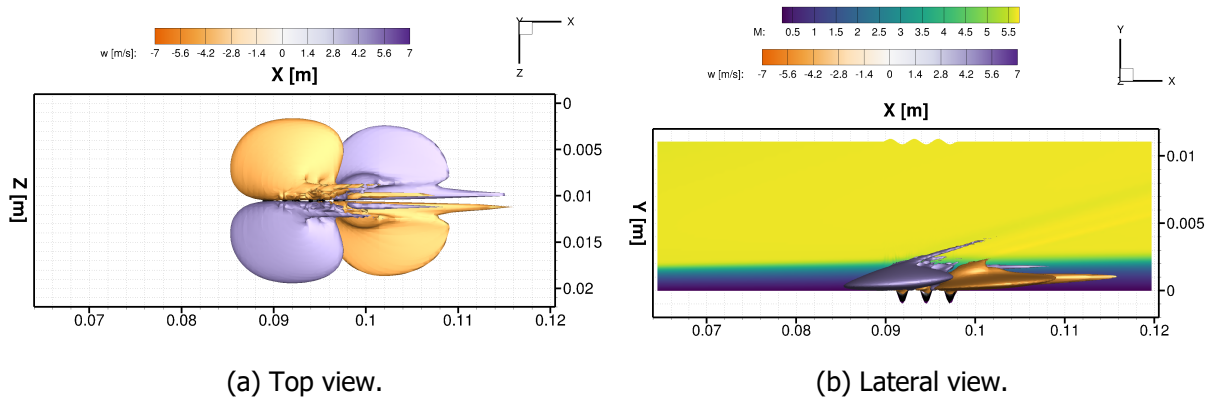

(a) Top view.

(b) Lateral view.

Fig 8. Spanwise-velocity iso-surfaces (w = ± 5 m/s). In the lateral view, the centreline slice shows the Mach field in the immediate vicinity of the roughness patch.
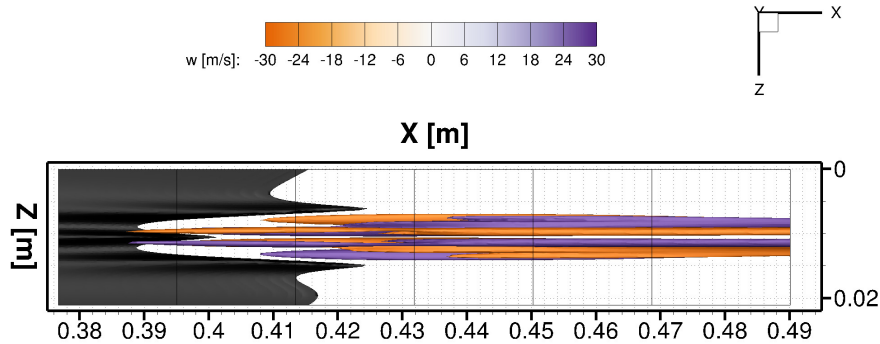
Fig 9. Spanwise-velocity iso-surfaces (w = ± 28 m/s) showing the stronger vortices downstream of reattachment.
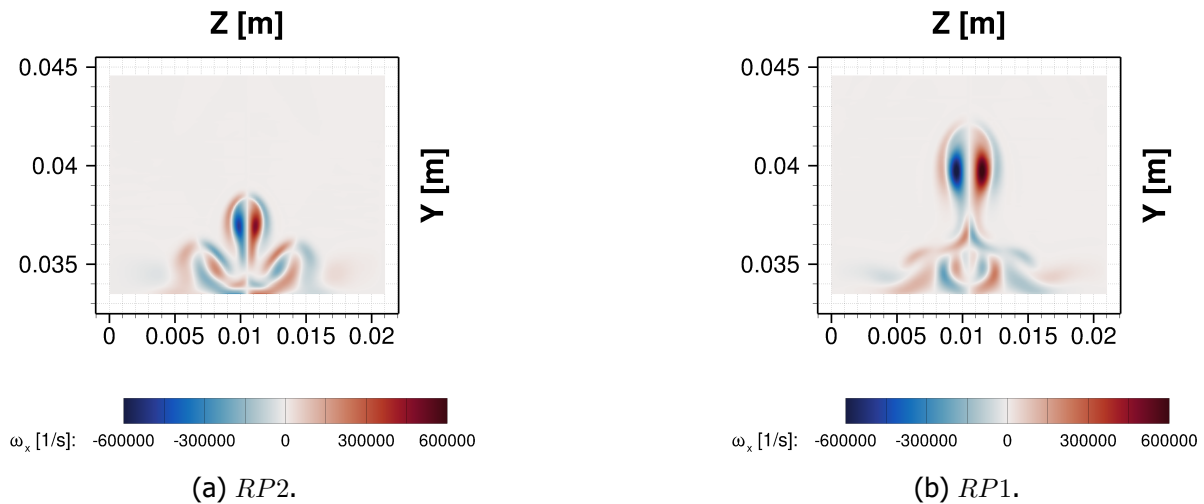

(a) $RP2$.

(b) $RP1$.

Fig 10. Streamwise vorticity at the end of the ramp for cases $RP2$ and $RP1$.

4.2.3. RP2B

In this case, the roughness elements cover the entire span of the domain. The streamwise position and Re_{kk} are the same as case $RP2$. The separation line again shows corrugations. However, due to the periodic nature of the patch, the separation point ($x_s \simeq 0.157$ m) is slightly delayed with respect to the single-element case, leading to a slightly earlier reattachment and a smaller bubble. In case $RP2B$, five mushroom structures develop on the ramp, as many as the roughness wavenumber in spanwise direction. The centre of each structure is aligned with the first streamwise hills (and therefore the last valleys) of the patch, as in case $RP2$. The downstream development of a single structure is affected by the two adjacent structures at its sides (Fig. 11a). As a consequence, while the core of each of the five structures is still $\Delta z^C \simeq 3.3$ mm, their width at the wall is limited to $\Delta z^W \simeq 4.2$ mm, which corresponds to twice the length of a spanwise wavelength (2.1 mm), as seen in Fig. 12a. Moreover, it can be noticed that the levels of streamwise vorticity characterizing the vortices core are lower with respect to case $RP2$. Finally, more numerous and narrower hot streaks are visible in the wall-temperature distribution, one per each vortex. However, the peak temperature $T_w \simeq 1692$ K is slightly lower than in the reference case.
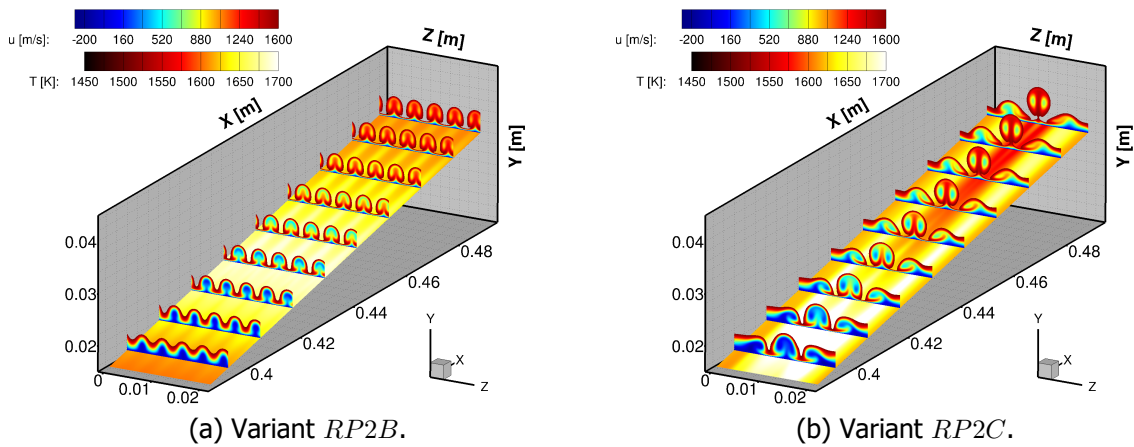
(a) Variant $RP2B$.

(b) Variant $RP2C$.

Fig 11. Variants $RP2B$ and $RP2C$. Evolution of the mushroom-shaped structure along the ramp (streamwise-velocity slices cut above u = 1600 m/s) and wall-temperature distribution.

4.2.4. RP2C

This case is again characterized by the same Re_{kk} value of the reference $RP2$. However, the wider 3-elements patch has an effect very similar to that of case $RP1$. The wake of the roughness is wider and shows higher vorticity levels with respect to the reference case. Therefore, the flow separation is slightly delayed ($x_s \simeq 0.155$ m) and reattachment is anticipated on the ramp. The resulting mushroom structure is wider than case $RP2$, both at the wall ($\Delta z^W \simeq 20$ mm) and in the core of the double-vortex ($\Delta z^C \simeq 4.9$ mm). However, the overall strength of the core, measured through the streamwise-vorticity ω_x, is comparable to that measured for cases $RP2$ and $RP1$, but higher than case $RP2B$. The wider vortical structure on the ramp entails a larger hot streak at the wall. Furthermore, for the patch $RP2C$, the peak temperature is the highest for the investigated cases ($T_w \simeq 1730$ K). Finally, as visible from Fig. 11b, the disturbance introduced by this roughness configuration is such that the flow has partially lost its symmetry once on the ramp.
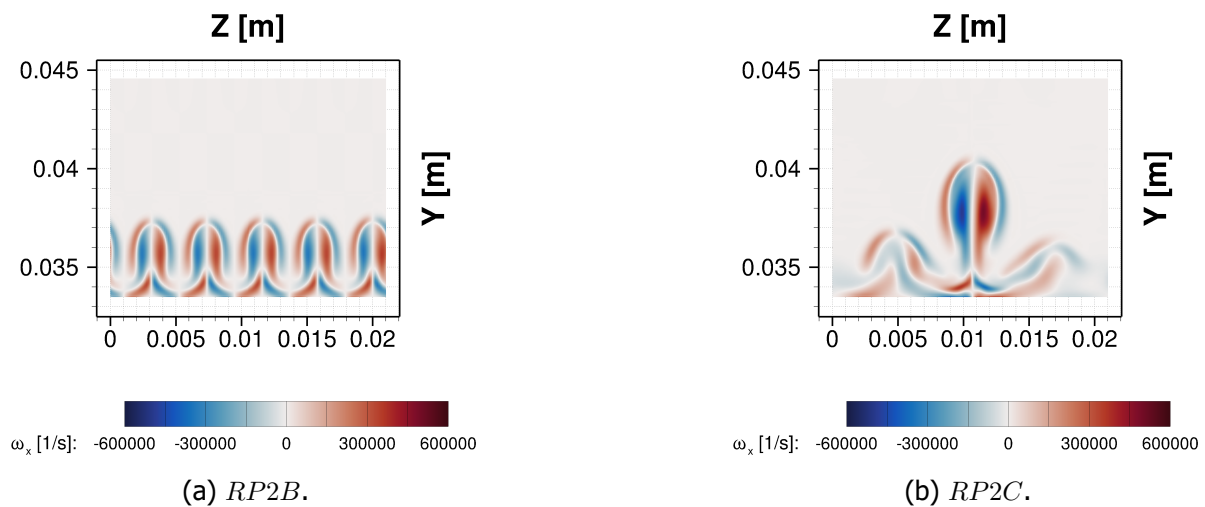

(a) $RP2B$.

(b) $RP2C$.

Fig 12. Streamwise vorticity at the end of the ramp for cases $RP2B$ and $RP2C$.

5. Conclusions

The study aimed at investigating the effects of several variants of a roughness patch placed in front of a 10° hypersonic ramp. The base version of the patch consisted of a single streamwise-row of sinusoidal elements placed upstream of the separation point for the smooth reference configuration. The patch generates streamwise vortices in its wake that are convected downstream on the separated shear layer and on the ramp. The separation is delayed with respect to the smooth case and both separation and reattachment lines show corrugations downstream of the roughness. As the wake flow reattaches on the ramp, a mushroom-shaped structure forms and dominates the weak streamwise vortices that are found in the smooth scenario. By moving the patch upstream or by making it wider, the boundary-layer exhibits a delayed separation and early reattachment on the ramp, together with a wider mushroom structure. This is believed to be a consequence of the higher roughness-induced vorticity generated by wider and/or more upstream patches. The case with a patch occupying the entire span of the domain has been also investigated. In this case, the boundary-layer detachment is again slightly delayed, but the vortical structures forming on the ramp (one per each spanwise roughness wavelength) are smaller and less intense with respect to the base version of the patch. In all the rough cases, the wall-temperature peak-values are remarkably higher than those of the smooth case, while the differences in maximum-temperature values among the patch variants are noticeable but not very large.

The present work shows how relatively small variations of the roughness parameters can have a noticeable impact on the steady base-flow of laminar Shock-Wave/Boundary-Layer Interaction. Under unsteady conditions, these modifications with respect to a smooth ramp-flow could promote the growth of disturbances introduced in the flow, leading to a faster laminar-turbulent transition process. Further investigations on this specific problem are therefore needed in the future.

6. ACKNOWLEDGEMENTS

References

1. Bertin, J.J., Cummings, R.M.: Critical hypersonic aerothermodynamic phenomena. Annual Review of Fluid Mechanics 38(1), 129–157 (2006)

2. Babinsky, H., Harvey, J.K.: Shock Wave–Boundary-Layer Interaction. Cambridge University Press (2011)

3. Korolev, G.L, Gajjar, J.S.B., Ruban, I.: Once again on the supersonic flow separation near a corner. Journal of Fluid Mechanics 463, 173–199 (2002)

4. Gai, S.L., Khraibut, A.: Hypersonic compression corner flow with large separated regions. Journal of Fluid Mechanics 877, 471–494, (2019)

5. Chiapparino, G., Stemmer, C.: Numerical investigation of a Mach 6 hypersonic laminar flow on two-dimensional cold-wall compression corners with controlled surface roughness. International Journal of Heat and Fluid Flow 94, 108937 (2022)

6. Burggraf, O.R.: Separated laminar boundary layers. Advances in Engineering Science. NASA Langley Research Center, 4 (1976)

7. Roghelia, A., Oliver, H., Egorov, I., Chuvakhov, P.: Experimental investigation of Görtler vortices in hypersonic ramp flows. Experiments in Fluids 58, 139 (2017)

8. Cao, S., Hao, J., Klioutchnikov, I., Olivier, H., Wen, C.Y.: Unsteady effects in a hypersonic compression ramp flow with laminar separation. Journal of Fluid Mechanics 912, A3 (2021)

9. Shrestha, P., Dwivedi, A., Hildebrand, N., Nichols, J.W., Jovanovic, M.R., Candler, G.V.: Interaction of an oblique shock with a transitional Mach 5.92 boundary layer. 46th AIAA Fluid Dynamics Conference (2016)

10. Hildebrand, N., Dwivedi, A., Nichols, J.W., Jovanovic, M.R., Candler, G.V.: Simulation and stability analysis of oblique shock-wave/boundary-layer interactions at Mach 5.92. Physical Review Fluids 3(1), 013906 (2018)

11. Liu, J.T.C.: Nonlinear instability of developing streamwise vortices with applications to boundary layer heat transfer intensification through an extended Reynolds analogy. Philosophical Transactions of the Royal Society 366, 2699–2716 (2008)

12. Holloway, P.F., Sterret, J.R.: Effect of controlled surface roughness on boundary-layer transition and heat transfer at Mach number of 4.8 and 6.0. TN D-2054, NASA (1964)

13. Hicks, R.M., Harper Jr., W.R.: A comparison of spherical and triangular boundary-layer trips on a flat plate at supersonic speeds. TM X-2146, NASA (1970)

14. Schneider, S.P.: Effects of roughness on hypersonic boundary-layer transition. Journal of Spacecraft and Rockets 45(2), 193–209 (2008)

15. King, R.A., Breuer, K.S.: Acoustic receptivity and evolution of two-dimensional and oblique disturbances in a Blasius boundary layer. Journal of Fluid Mechanics 432, 60–90 (2001)

16. De Tullio, N., Sandham, N.D.: Influence of boundary-layer disturbances on the instability of a roughness wake in a high-speed boundary layer. Journal of Fluid Mechanics 763, 136–165 (2014)

17. Van den Eynde, J.P., Sandham, N.D.: Numerical simulations of transition due to isolated roughness elements at Mach 6. AIAA Journal 54(1), 53–65 (2016)

18. Chou, A., King, R.A., Kegerise, M.A.: Transition induced by tandem rectangular roughness elements on a supersonic flat plate. AIAA Journal 54(8), 2322–2337 (2016)

19. Duan, L., Wang, X., Zhong, X.: A high-order cut-cell method for numerical simulation of hypersonic-boundary transition with arbitrary surface roughness. 47th AIAA Aerospace Sciences Meeting Including The New Horizons Forum and Aerospace Exposition (2009)

20. Poplavskaya, T.V., Kirilovskiy, S.V.: Numerical investigation of the influence of the structured surface on disturbance evolution and heat transfer in a hypersonic boundary layer. AIP Conference Proceedings 2027, 030019 (2018)

21. Paredes, P., Choudari, M.M., Li, F., Jewell, J.S., Kimmel, R.L., Marineau, E.C., Grossir, G.: Nosetip bluntness effects on transition at hypersonic speeds: Experimental and numerical analysis under NATO STO AVT-240. AIAA SciTech Forum (2018)

22. Hein, S., Theiss, A., Di Giovanni, A., Stemmer, C., Schilden, T., Schröder, W., Paredes, P., Choudhari, M.M., Li, F., Reshotko, E.: Numerical investigation of roughness effects on transition on spherical capsules. Journal of Spacecraft and Rockets 56(2), 388–404 (2019)

23. Di Giovanni, A., Stemmer, C.: Cross-flow-type breakdown induced by distributed roughness in the boundary layer of a hypersonic capsule configuration. Journal of Fluid Mechanics 856, 470–503 (2018)

24. Egorov, I.V., Novikov, V., Fedorov, A.V.: Direct numerical simulation of supersonic boundary layer stabilization using grooved wavy surface. 48th AIAA Aerospace Sciences Meeting Including the New Horizon Forum and Aerospace Exposition (2010)

25. Choudhari, M., Li, F., Edwards, J.: Stability analysis of roughness array wake in a high-speed boundary layer. 47th AIAA Aerospace Sciences Meeting (2009)

26.   Dwivedi, A., Sidharth, J., Nichols, J.W., Candler, G.V., Jovanovic, M.R.: Reattachment streaks in hypersonic compression ramp flow: an input-output analysis. Journal of Fluid Mechanics 880, 113–135 (2019)

27.   Wagner, A., Schramm, J.M., Wartemann, V., Camillo, G.P., Ozawa, H., Steelant, J.: Boundary layer transition studies on the HEXAFLY-INT hypersonic glide vehicle. FAR 2019 - International Conference on Flight Vehicls, Aerothermodynamics and Re-Entry Missions and Engineering, (2019)

28.   Vos, J., Duquesne, N., Lee, H.: Shock wave boundary layer interaction studies using the NSMB flow solver. 3rd European Symposium on Aerothermodynamics for Space Vehicles, ESA SP-426 (1999)

29.   Stemmer, C., Birrer, M., Adams, N.A.: Hypersonic boundary-layer flow with an obstacle in thermochemical equilibrium and nonequilibrium. Journal of Spacecraft and Rockets 54(4), 899–915 (2017)

30.   Stemmer, C., Birrer, M., Adams, N.A.: Disturbance development in an obstacle wake in a reacting hypersonic boundary layer. Journal of Spacecraft and Rockets 54(4), 945–960 (2017)